Proceedings of the ASME 2020 Dynamic Systems and Control Conference
DSCC 2020
October 4-7, 2020, Pittsburgh, Pennsylvania, USA

DSCC2020-24605

A NOVEL PLATE-LIKE SENSOR UTILIZING CURVATURE-BASED STIFFENING FOR NANOMETROLOGY APPLICATIONS

Rafiul Shihab, Tasmirul Jalil, Burak Gulsacan, Matteo Aureli, Ryan C. Tung *
Department of Mechanical Engineering
University of Nevada, Reno
Reno, Nevada 89557-0312

ABSTRACT

In this study, we propose a novel plate-like sensor which utilizes curvature-based stiffening effects for enhanced nanometrology. In the proposed concept, the stiffness and natural frequencies of the sensor can be arbitrarily adjusted by applying a transverse curvature via piezoelectric actuators, thereby enabling resonance amplification over a broad range of frequencies. The concept is validated using a macroscale experiment. Then, a microscale finite element analysis is used to study the effect of applied curvature on the microplate static stiffness and natural frequencies. We show that imposed transverse curvature is an effective way to tune the in-situ static stiffness and natural frequencies of the plate sensor system. These findings will form the basis of future curvature-based stiffening microscale studies for novel scenarios in atomic force microscopy.

INTRODUCTION

Measuring structural and material properties at the nanoscale is an important concern for the metrology community at large, as materials can exhibit different behaviors at the nanoscale when compared to their bulk characteristics [1, 2]. In recent years, Atomic Force Microscope (AFM) has become an indispensable tool to accurately predict material properties at the nanoscale [3, 4]. Some operating modes of AFM, including Scanning Joule Expansion Microscopy (SJEM), Electrochemical Strain Microscopy (ESM) and Piezoresponse Force Microscopy (PFM), have been utilized to measure minute surface displacements at particular excitation frequencies. To enhance microelectronic and nanoelectronic system capabilities, SJEM has been used to measure the thermal conductivity of thin films [5] and single walled carbon nanotubes [6]. SJEM has been further employed to assess the energy storage capability of various strains of *Streptomyces* bacteria [7]. In order to improve energy storage and generation in fuel cells and batteries, researchers have focused on electrochemical processes in different types of materials using Electrochemical Strain Microscopy (ESM). ESM is also used to measure surface deformations caused by ionic flows in a material, see [8–10]. Finally, Piezoresponse Force Microscopy (PFM) has been used to investigate piezoelectric and ferroelectric materials in oscillating electric fields [11] and to conduct surface displacement measurements on these materials. Each of the aforementioned techniques can be enhanced by utilizing the resonance behavior of the tip-sample system.

Contact resonance (CR) spectroscopy [12–19], a dynamic mode of AFM, uses resonance frequencies of the tip-sample system to accurately measure nanomechanical material properties. CR spectroscopy operates at or near the discrete natural frequencies of vibration of the permanently coupled tip-sample system. CR spectroscopy techniques can be combined with the aforementioned advanced AFM contact modes to produce higher fidelity measurements. For instance, pairing CR with PFM [20–22] has demonstrated considerable performance enhancement due to resonance amplification. Despite advantages of CR methods, the amplification bandwidth of the measurement is limited to the bandwidth of the discrete natural frequencies of the system. These natural frequency locations can also change due to changes in sample topography and local material properties. In other words, in traditional resonance amplification techniques, measurement of frequency-dependent data can only be acquired in narrow frequency bands, in proximity to the system resonances. In contrast, if controlled modulation of the resonance frequencies (and thus of the narrow sensing bands) is achievable, one will be able to accomplish resonance amplification in wide frequency bands.

*Address all correspondence to this author; rtung@unr.edu.

Resonance amplification at arbitrary frequencies can be accomplished by regulating the stiffness of the sensor *in-situ*. Mechanical or electromechanical methods can be implemented to obtain the adjustment of the sensor stiffness. Some mechanical methods include: changing the effective length of the resonating beam [23–25], using thermal input to change the temperature dependent Young's modulus [26], applying thermal stresses on the structure [27], and altering the shape of the device. Kawai et al. [28] applied a shape-changing strategy by designing a complex, fold-able device geometry using piezoelectric structures to vary the device stiffness. They folded a MEMS beam, which changed the second moment of area of the beam, and recorded a 14% difference in the static stiffness between the un-folded and folded states.

In a recent study by Aureli et al. [29], a plate sensor has been implemented to increase the sensor bandwidth, when compared to traditional narow beam sensor geometries. In this paper, we propose combining the method of Aureli et al. with curvature-induced in-plane straining on a continuous plate geometry. This will enable us to adjust the in-situ static and dynamic stiffness of the sensor across a wide range of frequencies. This work is inspired by the *Theorema Egregium* [30] of Gauss which states that the initial Gaussian curvature of a surface, defined as the product of two principal curvatures of the surface, remains the same when the material is undergoing a transformation that does not result in compressing or stretching of the structure. This phenomena can be observed in uniaxial bending of a narrow beam experiencing small displacement. Contrary to uniaxial bending, biaxial bending generates in-plane straining. Pini et al. [31] observed that the stiffness of a cantilevered plate is dramatically increased due to an applied transverse curvature and induced in-plane straining.

In the remainder of the paper, the concept of curvature-based stiffening is investigated in the context of nanometrology applications. First, to validate and demonstrate the feasibility of the concept, a macroscale experiment on a steel plate deformed by a bi-morph piezoelectric actuator is performed. Then, the effect of imposed transverse curvature via piezoelectric materials on the natural frequencies and static stiffness of the microplate sensor is analyzed in a FEM study.

EXPERIMENTAL STUDY

Macroscale Experiment

In this section, we describe a macroscale experiment performed to validate the effects of transverse curvature on the vibration characteristics of a cantilever plate. The schematic of this experiment is depicted in Fig. 1. Experiments are conducted on a carbon steel (AISI 1080) plate with a total length $L_t = 154$ mm, effective length $L = 104$ mm, width $b = 104$ mm, and thickness $h = 0.254$ mm. To enforce proper cantilever boundary conditions, two rigid aluminum plates are used to cover one end of the test plate. The cantilever plate is mounted on an electromagnetic shaker which provides base excitation to the plate. Transverse curvature is imposed by a bi-morph actuator built from two Macro-Fiber Composite (MFC) piezoelectric actuators, model

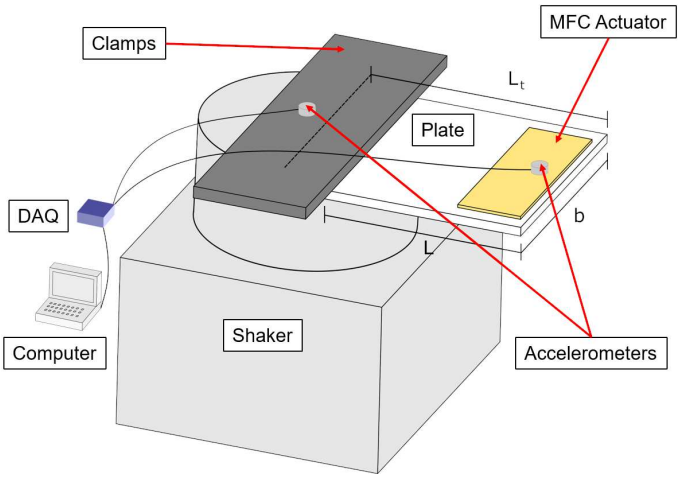

FIGURE 1. Schematics of experimental setup with the primary plate dimensions.

M8528-P1, produced by Smart Material Corp., at the free end of the cantilever plate. This bi-morph is used at a constant input voltage of 1500 V or with no actuation input which is referred to "Actuator ON" and "Actuator OFF" cases respectively, in the remainder of the study. Two accelerometers are mounted at the base and the tip of the plate to measure transverse vibration of the cantilever plate. Signals from the accelerometers are collected by a digital acquisition system (DAQ) and further post-processed to estimate the frequency response function (FRF) of the system between the tip acceleration and the base acceleration of the plate. The vibration excitation, for both Actuator ON and Actuator OFF cases, consists of 40 consecutive sweeps over a period of 10 s each of an input chirp sine excitation with a frequency range between 0.1 Hz and 100 Hz. Data are acquired with a custom VI in LabVIEW a sampling frequency of 2000 Hz.

The FRF of the system is generated with the "Dual Channel Spectral Measurement" routine block in the custom VI. The FRFs obtained from each of the 40 runs are averaged and the results are demonstrated in Fig. 2. The peak values in the FRF are used to identify the natural frequencies of the plate. The first prominent peak in the response reveals a global cantilever-like first bending mode for both the Actuator ON and Actuator OFF cases. A blue shift from 12.2 Hz to 12.8 Hz can be seen in the natural frequencies which results in an increase of approximately 4.9% in the value of the first natural frequency. The main reason behind this frequency shift can be attributed to the imposed curvature from the bi-morph actuator. Image analysis of pictures of the bent plate demonstrates that the actuator can impart a radius of curvature of approximately $R_c = 1192$ mm and non-dimensional curvature parameter of $\kappa = b/R_c = 0.087$. Although the magnitude of the imposed curvature is not large, the blue shift in natural frequency is significant and establishes a macroscale proof-of-concept for the tunability of AFM sensors via externally imposed curvature.

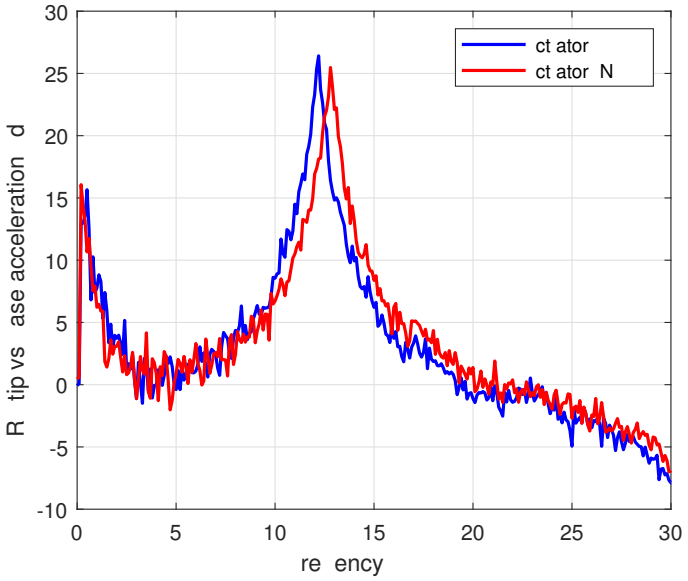

FIGURE 2. FRF between the cantilever plate tip and base excitation acceleration, for the actuator ON and actuator OFF cases.

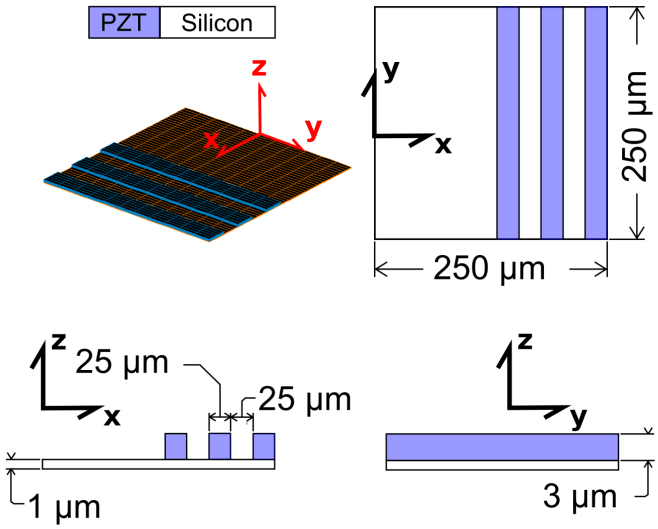

FIGURE 3. Geometry of the plate sensor used in the finite element analysis.

NUMERICAL STUDY

A three-dimensional finite element analysis of the proposed micro-sensor is performed in place of actually fabricating the device and performing AFM experiments. For the analysis, a microscale silicon plate with aspect ratio (length/width) 1 is taken and three strips of lead zirconate titanate (PZT) are placed at the free end of the plate for actuation. The PZT strips are placed in such a configuration that maximizes curvature in the desired direction and minimizes curvatures in the competing directions of the plate. The geometry and the properties of the elements used in the model can be found in Fig. 3 and Table 1.

Three-dimensional brick elements are used to mesh both the silicon plate and PZT strips. A fixed boundary condition (no displacement and rotation) is assumed at the left edge of the plate (at $x = 0$), and the remaining edges are free. To perform actuation, various input voltages are applied on the top faces of the PZT strips normal to the xy-plane, while the contacting faces between the plate and the PZT elements are kept at zero voltage. A linear spring element is assumed to model the sample contact, and it is placed on the optimum tip location of the plate. The optimum tip location in terms of optimal measurement sensitivity and modal density is given by Aureli et al. [29]. The sensitivity is defined by the rate of change of the contact natural frequencies for a unit increase in nondimensional sample stiffness. The optimum tip location is $x = 0.91L$ and $y = 0.4b$, where $x = 0$ is the fixed end and $y = 0$ is the center line of the plate.

In the first phase of the numerical study, we determine the static stiffness k_c of the cantilever plate by applying a small normal load F at $x = L$ and $y = 0$ on the deformed plate sensor and measuring the static displacement d. The static stiffness is then calculated using the relation $k_c = F/d$. Next, a static input voltage is applied on all three PZT strips to obtain the deformed static equilibrium configuration of the plate. This deformation leads to a transverse curvature and a longitudinal curvature in the plate. Moreover, due to these curvatures, the plate experiences a deflection in the z-direction. The direction of the transverse curvature is dependent on the polarity of the input voltage, and therefore, so is the deflection in the z-direction. The second phase of the numerical study includes performing a modal analysis on the static equilibrium configuration of the deformed (PZT active) system with a varying external sample spring stiffness (including zero stiffness) at the optimum tip location. These springs emulate contact with a measurement sample that would be experienced in actual contact resonance AFM experiments. In our study, we nondimensionalize the stiffness as $\alpha = k/k_c^0$ where α is the nondimensionalized stiffness, k is the assigned sample stiffness (linear spring), and k_c^0 is the static stiffness of the undeformed plate (see also [29]).

PZT Coefficients

The piezoelectric and dielectric properties of PZT materials dictate their stress and strain responses. These properties depend on numerous factors such as manufacturing techniques, grain size, film thickness and orientation, operating temperature, operating time, operating voltage, and the dimensions and geometry of the material [32–35]. Without experimental study, it is difficult to estimate piezoelectric stress and strain coefficients required for the FEM simulation as the values of the coefficients change nonlinearly as the transition from a PZT thick film to a thin film occurs. However, Shen et al. [32] introduced a calibration factor to compare the variation of theoretical piezoelectric

TABLE 1. Device material properties and dimensions. Here, the subscripts represent the material coordinate system, where $1 = x$, $2 = y$, $3 = z$, $4 = xy$, $5 = xz$, $6 = yz$.

	Stress Coefficient [N/Vm]	Strain Coefficient [m/V]	Young's Modulus [GPa]	Poisson's Ratio [-]	Shear Modulus [GPa]	Geometry		
						Length [μm]	Width [μm]	Thickness [μm]
PZT	e_{13} -7.21	d_{13} -1.85E-10	E_1 61	ν_{12} 0.35	G_{12} 22.6			
	e_{23} -7.21	d_{23} -1.85E-10	E_2 61	ν_{13} 0.38	G_{13} 21.1	250	25	3
	e_{33} 15.12	d_{33} 3.87E-10	E_3 53.2	ν_{23} 0.38	G_{23} 21.1	(Each Strip)	(Each Strip)	(Each Strip)
	e_{51} 12.33	d_{51} 5.84E-10						
	e_{62} 12.33	d_{62} 5.84E-10						
Silicon			E 169	ν 0.25		250	250	1

coefficients from the experimental values on the basis of substrate materials, boundary conditions, specimen size, thickness ratio, and specimen thickness. The largest deviation (250% increase) in the calibration factor found was due to the change in the thickness ratio (where the substrate thickness to PZT thickness ratio was 1:0.0029). The effect of changing the other parameters was not significant (less than 7%). In our FEM study, the silicon substrate to PZT thickness ratio is 1:3, so the calibration factor/deviation of the strain coefficient from the experimental values becomes negligible, and the bulk property values of PZT can be reasonably used during the simulation [32].

FEM Convergence

Meshing is performed using "ADINA" software [36], with 27 nodes per element and mapped or rule-based meshing. We performed the mesh convergence study by monitoring the following three aspects: a) the first eigenfrequency of the system, b) the static tip displacement of the device due to curvature, and c) the static tip displacement of the device due to an applied normal load. The convergence study has been conducted for the 50 V case, and convergence is considered to be achieved when changes in the aforementioned parameters are less than 0.25% upon doubling the number of elements. At the end of the study, for the silicon plate, we found the converged values (meeting the mentioned criteria) of length, width, and thickness subdivisions to be 50, 11, and 7, respectively, resulting in 3850 solid elements. For the PZT strip, the subdivision numbers are 5, 11, and 7 along its length, width, and thickness, respectively, resulting in 385 solid elements.

RESULTS AND DISCUSSIONS

Static Stiffness and Midpoint Deflection

The curvature applied through the piezoelectric strips contributes to the strain energy in the plate sensor, which changes the static stiffness of the plate. Figure 4 shows the numerically determined normalized static stiffness of the sensor versus input voltage to the piezoelectric strips. The normalized static stiffness

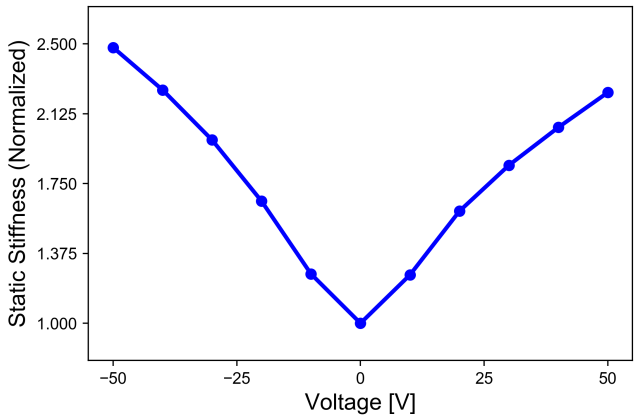

FIGURE 4. Static stiffness (bending) of the plate sensor, normalized by the stiffness of the undeformed plate, for different applied voltages. The stiffness of the device is increased approximately 2.5 times.

has been calculated by dividing all the static stiffness data by the 0 V static stiffness. For a $\pm$50 V input range, the static stiffness of the sensor is increased approximately 2.5 times the stiffness of the undeformed plate. Slight asymmetry can be observed in the dependence of the static stiffness for positive versus negative applied voltages. This asymmetry can be ascribed to a few causes. First, for plates undergoing longitudinal bending in a fixed direction, the change in the stiffness is dependent on the sign of the transverse curvature, see also [31]. Additional asymmetry might be introduced due to the one-sided placement of the piezoelectric strips, see Fig. 3.

The midpoint deflection is defined as the relative vertical displacement between the centerline and the free edges of the plate as shown in the inset of Fig. 5. Figure 5 also shows the nondimensional curvature κ of the sensor versus input voltage to the piezoelectric strips. Similar to the static stiffness, a small asymmetry can be observed in the midpoint deflection data for a positive versus negative applied voltage. The explanation of this midpoint deflection asymmetry is similar to that for the observed static stiffness asymmetry, that is, the direction of the cur-

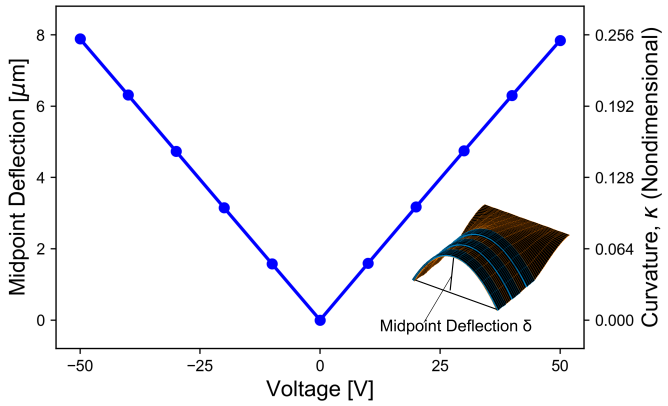

FIGURE 5. Midpoint deflection δ (not to scale in the inset) and corresponding nondimensional curvature parameter κ of the plate sensor for different applied voltages.

vature and the asymmetric placement of the piezoelectric actuators. The nondimensional curvature $\kappa = b/R_c$ has been calculated following the approach of Ahsan and Aureli [37], assuming a circular geometry of the curvature profile of the free end of the plate. With this assumption, the radius of curvature R_c can be defined as $R_c\theta = b/2$, where b is the width of the plate and θ is the sweep angle. Next, the midpoint deflection δ can be defined as $R_c(1-\cos\theta) = \delta$. Using both relationships, we obtain $(1/\kappa)(1-\cos(\kappa/2)) = \delta/b$, which can be further simplified by using a Maclaurin series and keeping terms up to second order. The final simplified relationship can be written as $\kappa \approx 8\delta/b$. Using this relation we can compare the κ values obtained from numerical simulation and experiment. The maximum nondimensional curvature observed in the simulations is approximately $\kappa = 0.25$ for the -50 V case. The macroscale experiment produces $\kappa = 0.087$. Approximately 34% of the total curvature in the experiment has been applied in the simulation.

Eigenfrequencies and Stiffness Sensitivity

In this section, we study the change in the natural frequency of the plate sensor with increasing applied curvature produced by applying an external voltage to piezoelectric actuators. The natural frequencies of the plate are calculated via modal analysis in the finite element software package. Figure 6 shows the corresponding natural frequencies of the first six eigenmodes of the plate as a function of the applied piezo voltage. Bending mode 1, 2, and 3 are identified in Fig. 6 as branch (a), (c), and (f), respectively. Both branch (b) and (d) are torsional modes and branch (e) is an eigenmode that resembles bending mode 3. Figure 6 also shows that each mode responds differently to the statically applied curvature and for some modes this change is significant. The most affected modes are better candidates for resonance amplification or dynamic stiffness tuning operations. Examining Fig. 6, we see that bending mode 1 displays a maximum frequency change of approximately 46%, bending mode 2 displays a maximum frequency change of approximately 198%,

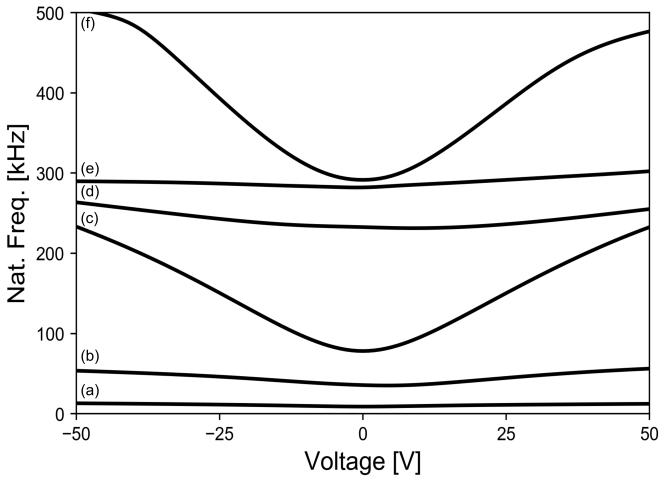

FIGURE 6. Calculated natural frequencies of the sensor for various input voltages (applied curvatures). Here bending mode 1, bending mode 2, and bending mode 3 is defined as branch (a), branch (c), and branch (f) respectively.

and bending mode 3 displays a maximum frequency change of approximately 73% for the voltage range tested. Table 2 shows the calculated natural frequency changes for the first three bending modes as a function of representative applied PZT voltages.

TABLE 2. Calculated natural frequencies vs. applied PZT voltage for bending mode 1, bending mode 2, and bending mode 3.

Voltage [V]	B1 [kHz]	B2 [kHz]	B3 [kHz]
-50	13.04	233.22	504.61
-25	11.39	150.61	393.29
0	8.90	78.19	291.55
25	11.08	150.35	386.66
50	12.38	232.60	476.73

Figure 7 shows the mode shapes of different bending modes for 0 and $+50$ V cases. Here, PZT voltage refers to the external input to the piezoelectric actuators attached to the plate sensor. It is clear from Fig. 7 that the change in curvature changes the mode shape in a complicated way. It is necessary to know which eigenmode the sensor is operating in for AFM applications, as the eigenmodes can affect the measurement significantly. In general AFM applications, the mode shape of the sensor is not determined and is assumed based on natural frequency values. If the mode shape is changed while applying different curvatures to the plate sensor, then the calculations will be erroneous. Thus, it is an absolute necessity to identify mode shapes at each voltage and corresponding natural frequency. An effective mode tracking method is needed to track the eigenmode which can compare

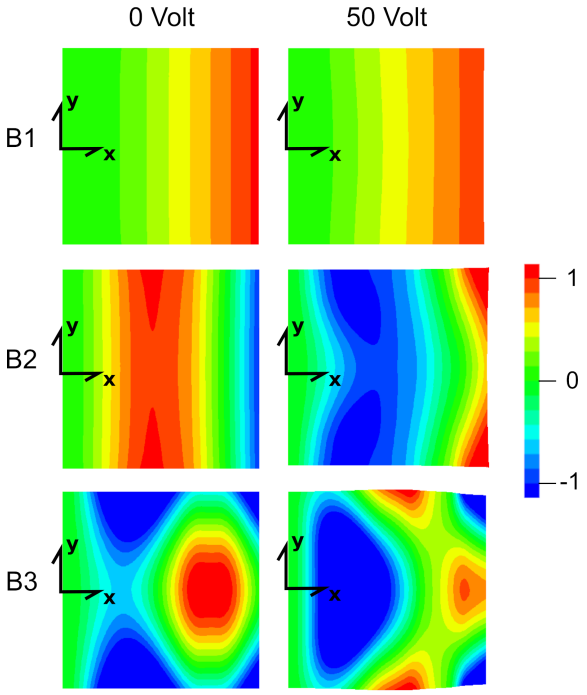

FIGURE 7. Mode shape of bending mode 1, bending mode 2, and bending mode 3 for 0 V and 50 V cases. Here, the clamped end is on the left edge of the plate and marked with a coordinate frame. The color bar depicts the maximum and minimum normalized z-eigenvector.

the mode shapes at each applied voltage to the 0 V case eigenmode and determine the current eigenmode for every voltage. This approach could be pursued by following for example the line of argument in [38]. However, this determination is outside the scope of the present exploratory study.

To use the proposed sensor in the context of contact resonance atomic force microscopy (CR-AFM), we study the effect of natural frequency change and natural frequency stiffness sensitivity $\mathrm{d}f/\mathrm{d}\alpha$ as a function of sample stiffness and applied voltage. Sample stiffness is represented by a single linear spring in the z-direction and placed in the aforementioned optimal tip location. The natural frequency and natural frequency sensitivity have been calculated for the non-dimensional stiffness range of $\alpha = 10^{-2}$ to $\alpha = 10^{6}$, where $\alpha = k/k_c^0$, k is the assigned sample stiffness, and k_c^0 is the static stiffness of the undeformed plate and the superscript 0 denotes the undeformed configuration.

Figure 8 shows the natural frequencies and natural frequency stiffness sensitivities vs. sample stiffness for two applied PZT voltages (0 and 50 volts) and three bending modes of the system, at the optimal sensor tip location mentioned above. It is clear from Fig. 8 that applied voltage, and thus sensor curvature, can be used to effectively tune the natural frequency of the device across a wide range of frequencies and sample stiffnesses. The sensitivity parameter $\mathrm{d}f/\mathrm{d}\alpha$ is a good indicator of the sensor performance for a specific sample stiffness, see for example the discussion in [29]. It is observed that the 50 V case has an increased sensitivity range, which enables us to capture stiffer sample properties. This effect can be used to achieve resonance amplification at desired frequencies and optimize the sensor static stiffness for a given sample stiffness. The effective stiffness detection range can be increased with applied curvature via external voltage application in the piezoelectric actuators, which can be controlled effectively. As seen from the Fig. 8 at PZT voltage of 50V, the stiffness detection range is extended significantly.

As the voltage is increased, the optimal tip location is expected to change position. In future studies, we would like to explore the evolution of optimal tip location for a given device curvature. Additionally, as seen in Fig. 8 (b), it is possible for the tip location to coincide or get close to a nodal vibration line and reduce the stiffness sensitivity. This is observed in the 50 V actuation case for bending mode 2 at the optimal tip location.

Finally, as the sensor stiffness is increased, the overall stiffness sensitivity $\mathrm{d}f/\mathrm{d}\alpha$ of each bending mode decreases with respect to the undeformed sensor. This is expected, and predicted by a simple one-dimensional model. Let the natural vibration frequency be given by $f = \frac{1}{2\pi}\sqrt{\frac{k_{\text{eff}}}{m_{\text{eff}}}}$, where k_{eff} and m_{eff} are the effective stiffness and mass of the lumped-parameter model. Then, the frequency sensitivity with respect to stiffness is given by $\frac{df}{dk_{\text{eff}}} = \frac{1}{4\pi}\sqrt{\frac{1}{m_{\text{eff}}}}\sqrt{\frac{1}{k_{\text{eff}}}}$. As the effective stiffness or mass of the system increases, the frequency sensitivity to stiffness decreases. Therefore, we do not expect that making the sensor as stiff as possible is an optimal strategy. Rather, the value of our work is to allow arbitrary adjustment of the sensitivity of the system.

Practical Limitations

Determining the allowable stresses in different directions of the plate and the PZT strips is one of the major challenges in a practical implementation of the device. The structural limit of the system is determined by the following aspects: a) the maximum axial stress in the plate and PZT, and b) the maximum shear stress between the plate and the PZT. The axial stress must be less than what the silicon or PZT material can withstand. Similarly, the interfacial bond strength between the PZT and silicon must be higher than the shear stress between the PZT strips and silicon plate to prevent delamination of the PZT elements from the plate. Therefore, to determine the maximum stresses experienced by the device, three-dimensional structural FEM simulations are performed for 10 V to 50 V applied voltages with 10 V increments. Table 3 shows the maximum axial and shear stresses in the device at various input voltages. The stress distributions of the silicon plate under the applied voltage of 50 V can be found in Figure 9. Here, σ_{xx} and σ_{yy} represent the axial stress of the plate and PZT and σ_{xz} and σ_{yz} represent the shear stress between the plate and the PZT strips. The ultimate tensile strength of monocrystalline silicon is well known (7 GPa) [39], suggesting that the silicon plate is safely operable to the maximum range of the applied voltage (Table 3). Determining the property for PZT ceramics is more complicated, especially within the range of our operating thickness (3 μm). Therefore, there should be an optimization between the required actuation from the device and

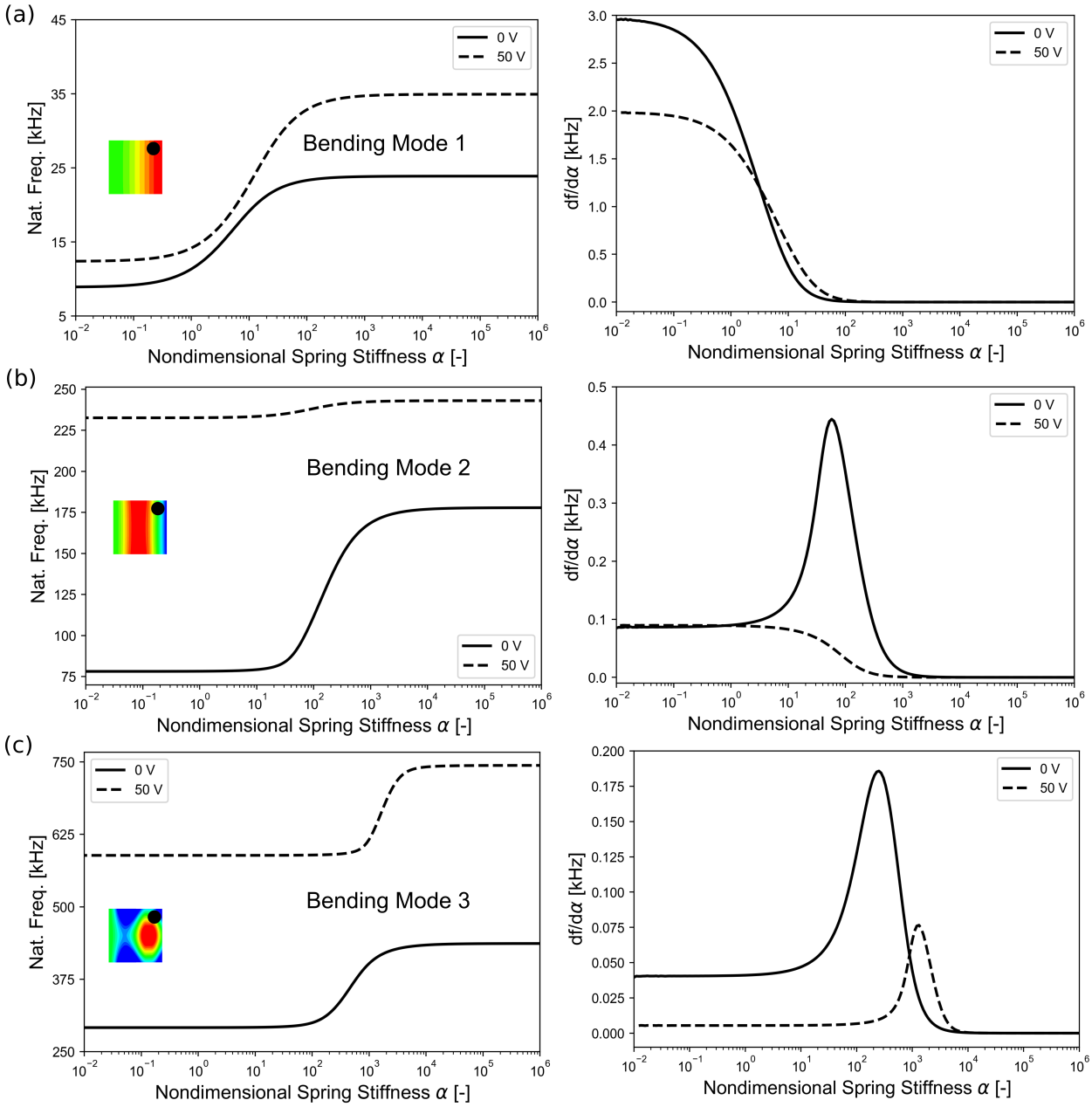

FIGURE 8. Natural frequencies and natural frequency stiffness sensitivities vs. sample stiffness for various PZT voltages at the optimum tip location. Inset images depict the eigenmodes of vibration at 0V. The spring location is indicated by the black dot in the inset images.

structural endurance of the PZT material in terms of allowable voltage input. The maximum allowable voltage across the PZT strip is dependent on the dielectric breakdown strength of the PZT material. The dielectric breakdown strength can be adjusted by using different fabrication techniques. For instance, recently, Ko et al. [40] reported a method of adjusting the amount of Pb excess in PZT thin film actuators and improved the dielectric breakdown strength from 300 kV/cm to 1 MV/cm facilitating a range of allowable input voltage for actuation. The measurement of interfacial bond strength between the PZT and silicon of the device is a very difficult task especially for the thin films [41]. From our FEM analysis, we found the maximum shear stress developed between the plate and PZT strips is $\sigma_{xz} = 102.85$ MPa for a 50 V input voltage (see Table 3). The value of the developed shear stress will vary depending on the voltage applied to the device. Experimental study must be conducted to assure that the interfacing method used in fabricating the device is capable of providing the required interfacial bond strength to prevent delamination of the PZT strips from the silicon plate. For instance, Berfield et al. [41] used a non-contact laser spallation method to

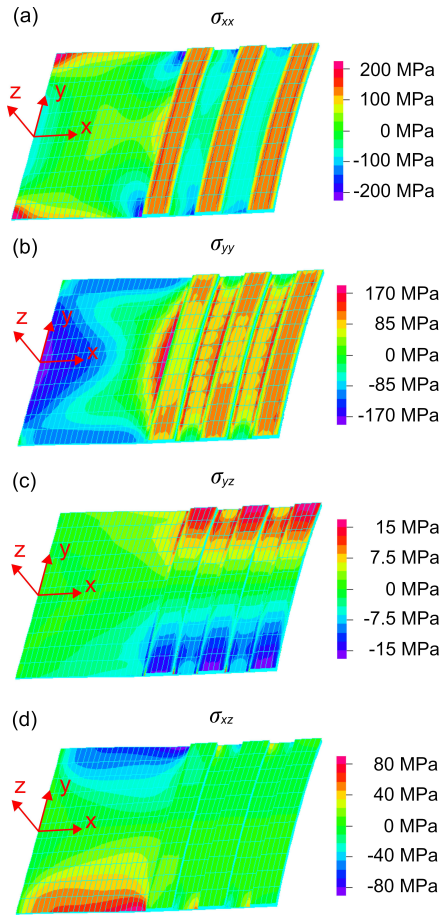

FIGURE 9. Numerically calculated system stresses at +50 V. (a) Axial stress σ_{xx} in the x direction, (b) axial stress σ_{yy} in the y direction, (c) shear stress σ_{yz} in the yz direction, (d) shear stress σ_{xz} in the xz direction.

deposit PZT sol-gel thin films on a silicon based substrate. They found the substrate-PZT interfacial strength to be in the range of 460 to 480 MPa. Therefore, we can reasonably assume that the plate-PZT interface is physically realizable, regardless of experimental challenges.

TABLE 3. Axial and shear stresses acting on the device components.

Voltage [V]	Axial Stresses Silicon [MPa]		Axial Stresses PZT [MPa]		Shear Stresses Whole Device [MPa]	
	σ_{xx}	σ_{yy}	σ_{xx}	σ_{yy}	σ_{xz}	σ_{yz}
10	63.93	51.62	50.05	51.74	21.25	10.61
20	134.80	102.73	99.72	102.65	42.64	23.43
30	211.43	154.65	149.49	152.62	63.54	38.50
40	291.22	207.11	199.52	201.41	83.65	55.66
50	372.58	259.72	249.87	248.84	102.85	74.79

CONCLUSIONS

In this work, a curvature-based, *in-situ* stiffness tunable, AFM plate sensor has been presented. A macroscale experiment has been conducted to demonstrate the effects of curvature on the resonance frequencies of the plate and a 4.9% shift in the first natural frequency has been observed. A finite element analysis was then conducted with a microscale sensor system to show the curvature induced stiffening effect on the plate sensor and the effect of the applied curvature on the resonant frequencies. We observed that the curvature applied to the sensor via microscale piezoelectric actuators changes the resonance frequencies and allows us to increase the static stiffness of the sensor by approximately 2.5 times. This work is the first step to formulate and construct a novel plate-like sensor based on the curvature stiffening effect. This effect can be used to significantly improve nanomaterial characterization and thus advance several nanometrology applications.

ACKNOWLEDGMENTS

This material is based in part upon work supported by the National Science Foundation under grant CMMI-1660448 (to RCT) and grant CMMI-1847513 (to MA). The authors would like to thank Navid Forootan for his help with the experiments.

REFERENCES

[1] Boukai, A. I., Bunimovich, Y., Tahir-Kheli, J., Yu, J.-K., Goddard Iii, W. A., and Heath, J. R., 2008. "Silicon nanowires as efficient thermoelectric materials". *Nature,* **451**(7175), pp. 168–171.

[2] Yan, L., Zhao, F., Li, S., Hu, Z., and Zhao, Y., 2011. "Low-toxic and safe nanomaterials by surface-chemical design, carbon nanotubes, fullerenes, metallofullerenes, and graphenes". *Nanoscale,* **3**(2), pp. 362–382.

[3] Hurley, D. C., 2009. "Contact resonance force microscopy techniques for nanomechanical measurements". In *Applied Scanning Probe Methods XI*. Springer, pp. 97–138.

[4] Farahi, R., Charrier, A. M., Tolbert, A., Lereu, A. L., Ragauskas, A., Davison, B. H., and Passian, A., 2017. "Plasticity, elasticity, and adhesion energy of plant cell walls: nanometrology of lignin loss using atomic force microscopy". *Scientific Reports,* **7**(1), pp. 1–12.

[5] Gurrum, S. P., King, W. P., Joshi, Y. K., and Ramakrishna, K., 2008. "Size effect on the thermal conductivity of thin metallic films investigated by scanning joule expansion microscopy". *Journal of Heat Transfer,* **130**(8), p. 082403.

[6] Song, J., Lu, C., Xie, X., Li, Y., Zhang, Y., Grosse, K. L., Dunham, S., Huang, Y., King, W. P., and Rogers, J. A., 2013. "Thermomechanical modeling of scanning joule expansion microscopy imaging of single-walled carbon nanotube devices". *Journal of Applied Mechanics,* **80**(4), p. 040907.

[7] Deniset-Besseau, A., Prater, C. B., Virolle, M., and Dazzi,

A., 2014. "Monitoring TriAcylGlycerols accumulation by atomic force microscopy based infrared spectroscopy in streptomyces species for biodiesel applications". *The Journal of Physical Chemistry Letters,* **5**(4), pp. 654–658.

[8] Luchkin, S. Y., Romanyuk, K., Ivanov, M., and Kholkin, A. L., 2015. "Li transport in fresh and aged $LiMn_2O_4$ cathodes via electrochemical strain microscopy". *Journal of Applied Physics,* **118**(7), p. 072016.

[9] Amanieu, H.-Y., Thai, H. N., Luchkin, S. Y., Rosato, D., Lupascu, D. C., Keip, M.-A., Schröder, J., and Kholkin, A. L., 2015. "Electrochemical strain microscopy time spectroscopy: Model and experiment on $LiMn_2O_4$". *Journal of Applied Physics,* **118**(5), p. 055101.

[10] Yang, S., Wu, J., Yan, B., Li, L., Sun, Y., Lu, L., and Zeng, K., 2017. "Nanoscale characterization of charged/discharged lithium-rich thin film cathode by scanning probe microscopy techniques". *Journal of Power Sources,* **352**, pp. 9–17.

[11] Balke, N., Bdikin, I., Kalinin, S. V., and Kholkin, A. L., 2009. "Electromechanical imaging and spectroscopy of ferroelectric and piezoelectric materials: State of the art and prospects for the future". *Journal of the American Ceramic Society,* **92**(8), pp. 1629–1647.

[12] Rabe, U., and Arnold, W., 1994. "Acoustic microscopy by atomic-force microscopy". *Applied Physics Letters,* **64**(12), pp. 1493–1495.

[13] Hurley, D. C., Kopycinska-Muller, M., and Kos, A. B., 2007. "Mapping mechanical properties on the nanoscale using atomic-force acoustic microscopy". *The Journal of The Minerals, Metals & Materials Society,* **59**(1), pp. 23–29.

[14] Killgore, J. P., Yablon, D. G., Tsou, A. H., Gannepalli, A., Yuya, P. A., Turner, J. A., Proksch, R., and Hurley, D. C., 2011. "Viscoelastic property mapping with contact resonance force microscopy". *Langmuir,* **27**(23), pp. 13983–13987.

[15] Rezaei, E., and Turner, J. A., 2017. "Contact resonance AFM to quantify the in-plane and out-of-plane loss tangents of polymers simultaneously". *Applied Physics Letters,* **110**(10), p. 101902.

[16] Gonzalez-Martinez, J. F., Kakar, E., Erkselius, S., Rehnberg, N., and Sotres, J., 2019. "Effect of relative humidity on the viscoelasticity of thin organic films studied by contact thermal noise AFM". *Langmuir,* **35**(18), pp. 6015–6023.

[17] Fiedler-Higgins, C. I., Cox, L. M., DelRio, F. W., and Killgore, J. P., 2019. "Monitoring fast, voxel-scale cure kinetics via sample-coupled-resonance photorheology". *Small Methods,* **3**(2), p. 1800275.

[18] Killgore, J. P., Deolia, A., Robins, L., and Murray, T. W., 2019. "Experimental reconstruction of the contact resonance shape factor for quantification and amplification of bias-induced strain in atomic force microscopy". *Applied Physics Letters,* **114**(13), p. 133108.

[19] Marinello, F., Passeri, D., and Savio, E., 2012. *Acoustic scanning probe microscopy*. Springer Science & Business Media.

[20] Jesse, S., Mirman, B., and Kalinin, S. V., 2006. "Resonance enhancement in piezoresponse force microscopy: Mapping electromechanical activity, contact stiffness, and Q factor". *Applied Physics Letters,* **89**(2), p. 022906.

[21] Kofahl, C., Güthoff, F., and Eckold, G., 2019. "Direct observation of polar nanodomains in the incommensurate phase of $(K_{0.96}Rb_{0.04})_2ZnCl_4$ crystals using piezo force microscopy". *Ferroelectrics,* **540**(1), pp. 10–17.

[22] Zhu, Q., Pan, K., Xie, S., Liu, Y., and Li, J., 2019. "Nanomechanics of multiferroic composite nanofibers via local excitation piezoresponse force microscopy". *Journal of the Mechanics and Physics of Solids,* **126**, pp. 76–86.

[23] Zine-El-Abidine, I., and Yang, P., 2009. "A tunable mechanical resonator". *Journal of Micromechanics and Microengineering,* **19**(12), p. 125004.

[24] Mueller-Falcke, C., Song, Y.-A., and Kim, S.-G., 2004. "Tunable stiffness scanning microscope probe". In Optomechatronic Micro/Nano Components, Devices, and Systems, Vol. 5604, International Society for Optics and Photonics, pp. 31–38.

[25] Mueller-Falcke, C., Gouda, S. D., Kim, S., and Kim, S.-G., 2006. "A nanoscanning platform for bio-engineering: an in-plane probe with switchable stiffness". *Nanotechnology,* **17**(4), p. S69.

[26] Zhang, H. J., and Qiu, C. J., 2006. "Characterization and MEMS application of low temperature TiNi(Cu) shape memory thin films". *Materials Science and Engineering: A,* **438**, pp. 1106–1109.

[27] Syms, R. R. A., 1998. "Electrothermal frequency tuning of folded and coupled vibrating micromechanical resonators". *Journal of Microelectromechanical Systems,* **7**(2), pp. 164–171.

[28] Kawai, Y., Ono, T., Meyers, E., Gerber, C., and Esashi, M., 2006. "Piezoelectric actuator integrated cantilever with tunable spring constant for atom probe". In Micro Electro Mechanical Systems, 2006. MEMS 2006 Istanbul. 19th IEEE International Conference on, IEEE, pp. 778–781.

[29] Aureli, M., Ahsan, S. N., Shihab, R. H., and Tung, R. C., 2018. "Plate geometries for contact resonance atomic force microscopy: Modeling, optimization, and verification". *Journal of Applied Physics,* **124**(1), p. 014503.

[30] Gauss, K. F., 1902. *General investigations of curved surfaces of 1827 and 1825*.

[31] Pini, V., Ruz, J. J., Kosaka, P. M., Malvar, O., Calleja, M., and Tamayo, J., 2016. "How two-dimensional bending can extraordinarily stiffen thin sheets". *Scientific Reports,* **6**.

[32] Guo, Q., Cao, G., and Shen, I., 2013. "Measurements of piezoelectric coefficient d_{33} of lead zirconate titanate thin films using a mini force hammer". *Journal of Vibration and Acoustics,* **135**(1), p. 011003.

[33] Haccart, T., Cattan, E., and Remiens, D., 2002. "Dielectric, ferroelectric and piezoelectric properties of sputtered PZT thin films on Si substrates: influence of film thickness and

orientation". *Semiconductor Physics Quantum Electronics & Optoelectronics*.

[34] Kurchania, R., and Milne, S., 1999. "Characterization of sol-gel $Pb(Zr_{0.53}Ti_{0.47})O_3$ films in the thickness range 0.25–10 μm". *Journal of Materials Research,* **14**, 05, pp. 1852 – 1859.

[35] Nam, H.-J., Kim, H.-H., and Lee, W.-J., 1998. "The effects of the preparation conditions and heat-treatment conditions of $Pt/Ti/SiO_2/Si$ substrates on the nucleation and growth of $Pb(Zr,Ti)O_3$ films". *Japanese Journal of Applied Physics,* **37**(6R), p. 3462.

[36] R & D Inc., A., 2018. *ADINA 9.4 Manuals*. www.adina.com, Watertown, MA 02472 USA.

[37] Ahsan, S. N., and Aureli, M., 2017. "Nonlinear oscillations of shape-morphing submerged structures: Control of hydrodynamic forces and power dissipation via active flexibility". *Journal of Fluids and Structures,* **74**, pp. 35–52.

[38] Huang, J., Krousgrill, C. M., and Bajaj, A. K., 2006. "Modeling of automotive drum brakes for squeal and parameter sensitivity analysis". *Journal of Sound and Vibration,* **289**(1-2), pp. 245–263.

[39] Petersen, K. E., 1982. "Silicon as a mechanical material". *Proceedings of the IEEE,* **70**(5), pp. 420–457.

[40] Ko, S. W., Zhu, W., Fragkiadakis, C., Borman, T., Wang, K., Mardilovich, P., and Trolier-McKinstry, S., 2019. "Improvement of reliability and dielectric breakdown strength of Nb-doped lead zirconate titanate films via microstructure control of seed". *Journal of the American Ceramic Society,* **102**(3), pp. 1211–1217.

[41] Berfield, T. A., Kitey, R., and Kandula, S. S., 2016. "Adhesion strength of lead zirconate titanate sol-gel thin films". *Thin Solid Films,* **598**, pp. 230–235.